Armouring effect on Sr-Nd isotopes during disequilibrium crustal melting: the case study of frozen migmatites from El Hoyazo and Mazarrón, SE Spain

Giulia PERINI[1], Bernardo CESARE[2,3], María Teresa GÓMEZ-PUGNAIRE[4], Lorenzo GHEZZI[1] and Simone TOMMASINI[1,*]

[1] Università degli Studi di Firenze, Dipartimento di Scienze della Terra, Via La Pira 4, 50121 Firenze, Italy
*Corresponding author, e-mail: toms@unifi.it
[2] Università di Padova, Dipartimento di Geoscienze, via Giotto 1, 35137 Padova, Italy
[3] C.N.R., Istituto di Geoscienze e Georisorse, Sezione di Padova, Corso Garibaldi 37, 35137 Padova, Italy
[4] Universidad de Granada, Facultad de Ciencias and Instituto Andaluz de Ciencias de la Tierra (Consejo Superior de Investigaciones Científicas) Campus Fuentenueva, s/n, 18002 Granada, Spain

Abstract: Crustal melting is responsible for the production of large volumes of rhyolitic melt and therefore is central to understand the rheology of the crust and the mechanisms of crustal differentiation. The attainment of isotopic equilibrium during melting of crustal rocks is implicitly assumed in most isotopic dating and tracing studies. This assumption considers the melting event as an instantaneous process and does not take into account the duration of anatexis. To assess the critical role of the timescale of crustal melting, we have studied the unique occurrence of *erupted migmatites* enclosed as xenoliths in the El Hoyazo and Mazarrón dacites of the Neogene Volcanic Province of SE Spain. These xenoliths represent the residue after some 30–60 % rhyolitic melt extraction at *P-T* conditions of 5–7 kbar and ~850 °C, and consist of biotite, plagioclase, sillimanite, garnet, cordierite, graphite and abundant glass inclusions (*i.e.*, not extracted rhyolitic melt) within each mineral phase. The timescale of melt extraction was ~3 Myr and <0.8 Myr at El Hoyazo and Mazarrón, respectively, resembling the duration of melting events during rapid anatexis caused by basalt underplating and crustal assimilation processes.

In both localities, the minerals and glass inclusions of erupted migmatites preserve a significant Sr and minor Nd isotope disequilibrium. At Mazarrón the isotopic disequilibrium is most marked owing to the shorter residence time of the melt within the source. The isotopic disequilibrium is not caused by the major xenolith-forming minerals but rather by the accessory phosphate inclusions (apatite ± monazite ± xenotime) hosted in garnet and biotite. The preservation of isotopic disequilibrium in these accessory phases has been facilitated by both their intrinsically low Sr and Nd diffusion coefficients and the armouring effect caused by their occurrence within biotite and garnet crystals, which acted as chemical barriers to Sr and Nd diffusion. This result implies that modelling of radiogenic isotope equilibration in natural systems should consider elemental diffusion in a composite medium with a resistance at the interface, *i.e.* different partition coefficients between adjacent mineral phases.

Key-words: Sr-Nd isotope disequilibrium, element diffusion, crustal melting, erupted migmatite, Neogene Volcanic Province, Spain.

1. Introduction

The radiogenic isotope (Sr, Nd, Pb) composition of silicate melts derived from crustal sources, whose minerals did not attain isotopic equilibrium during high-T metamorphism and melting, is controlled by the relative proportion of each mineral phase entering the melt (Hammouda *et al.*, 1996; Tommasini & Davies, 1997; Knesel & Davidson, 2002 and references therein). In this context, apatite and monazite have an important role in shaping the Nd isotopic composition of anatectic melts, whilst Rb- and Sr-bearing minerals, such as micas and feldspars, contribute to determine their Sr isotope compositions (*e.g.*, Ayres & Harris, 1997;

Harris & Ayres, 1998; Zeng *et al.*, 2005a). Recent studies (Zeng *et al.*, 2005a, b and c) provide arguments that in natural crustal systems where isotope disequilibrium melting occurs, the Sr and Nd isotope composition of magmas is strictly dependent upon variations of physical parameters, such as temperature and fluid activity, which, in turn, influence the proportions of micas *versus* feldspars and apatite *versus* monazite entering the melt (Zeng *et al.*, 2005a). At high temperature and fluid-absent conditions, micas and apatite are generally reactants, and can potentially produce melts with Sr and Nd isotope signatures more radiogenic than their source rock; at lower temperature and fluid-fluxed conditions feldspars and monazite

dissolve easily in melting reactions and can potentially produce melts with Sr and Nd isotope signatures less radiogenic than their source rock.

The parameters controlling the extent of isotopic homogenisation during high temperature events are: (i) the time-scale elapsed from the attainment of minerals closure temperatures and the onset of melting, (ii) the rate of elemental diffusion between adjacent minerals or between minerals and melt phase, (iii) the extent of recrystallisation, (iv) the activity of fluids, (v) the rate of melting, (vi) the rate of melt extraction.

Experimental studies for the determination of elemental diffusion coefficients are generally made to simulate a mineral phase immersed in a diffusing homogeneous medium (*e.g.*, Giletti, 1991; Cherniak & Watson, 1992; Cherniak & Ryerson, 1993; Cherniak, 1996, 2000). However, observations on natural samples indicate that diffusion in solids (*i.e.*, rocks before melting) is unlikely to resemble experiments which consider diffusion in an infinite reservoir, and are strictly dependent on the nature of coexisting phases (*e.g.*, Burton *et al.*, 1995).

Accessory phases in the source rock may be dispersed throughout the solid assemblage, mainly at grain boundaries, or enclosed into major mineral phases. Indeed, in disequilibrium melting of the crust, accessory minerals such as apatite and monazite can either be capable of isotopic equilibration with solid and melt phases, or can be isolated from the surrounding assemblage by the armouring effect caused by the host-minerals. Therefore, the different microstructural distribution of REE-bearing accessory phases and the nature of surrounding phases can have a potentially great influence on the isotopic signature of anatectic melts. To address this issue, we analysed phosphates-bearing metapelitic restitic xenoliths hosted in high-K calc-alkaline volcanic rocks of El Hoyazo (1 sample) and Mazarrón (4 samples), which represent a rather unique example of *"erupted migmatite"* (Zeck, 1970). Major, trace elements as well as Sr and Nd isotope analyses have been performed on whole-rock xenoliths, mineral separates, and host-lavas.

2. Geological background

The El Hoyazo high-K calc-alkaline dacitic dome is located in the eastern border of the Betic Cordillera, and belongs to the Neogene Volcanic Province (NVP) of SE Spain, which extends from Cabo de Gata to Mazarrón and Cartagena (Fig. 1). The NVP, in turn, is part of a widespread magmatism that occurred in the Alboran region from Southern Spain to the Alboran Sea and Northern Morocco (Fig. 1) from the Eocene to the Pleistocene (Duggen *et al.*, 2004). The Betic Cordillera and the Rif of Morocco, which surround the Alborán Sea (Fig. 1), formed a unique orogenic system that developed during Late Cretaceous and Early Tertiary as result of the convergence between the African and Eurasian plates (Turner *et al.*, 1999 and references therein). The basement of the NVP is formed by Paleozoic metamorphic rocks
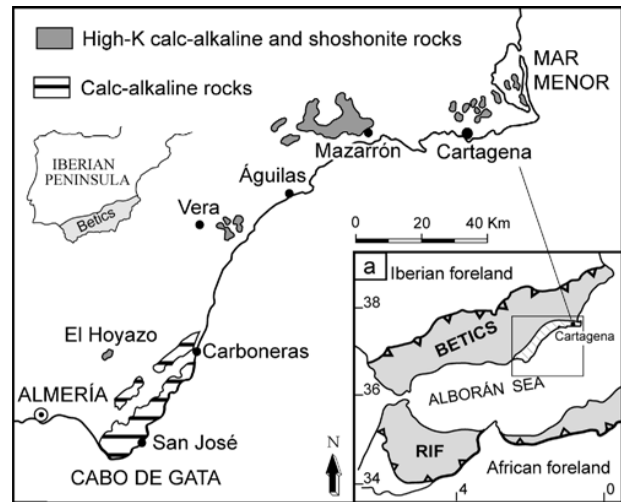

Fig. 1. Geological sketch map of the Neogene Volcanic Province of SE Spain showing the main outcrops of calc-alkaline and shoshonitic volcanic rocks (after Cesare *et al.*, 2003a) along a ca. 200 km NE–SW trending belt from Almeria to Mar Menor. Abundant restitic crustal xenoliths are ubiquitous in the dacitic lavas of the NVP. Inset: Tectonic map of the westernmost Mediterranean showing the schematic structure of the Betic Cordilleras-Rif system; the box indicates the area enlarged in the geological map with the diagonal pattern showing the Neogene Volcanic Province.

(Alpujárride, Maláguide and Nevado-Filábride Units) overlain by Miocene sediments. It has been thinned by an extensional tectonic phase starting in the Early Miocene that in the whole Alborán region resulted in an attenuated lithosphere thickness (Banda *et al.*, 1983; Torné *et al.*, 2000; Julià *et al.*, 2005).

The NVP comprises different magma series: calc-alkaline, high-K calc-alkaline (HKCA), shoshonitic, ultrapotassic and Na-alkaline (López-Ruiz *et al.*, 2002 and references therein). Magmatism of the NVP primarily lasted from Middle to Upper Miocene, with minor activity during the Pliocene (Turner *et al.*, 1999; Duggen *et al.*, 2004 and references therein). The Neogene HKCA dacites from SE Spain commonly contain metapelitic restitic xenoliths, which provide evidence for partial melting of the continental crust and represent the residuum after extraction of ~40 wt. % anatectic melt from a graphitic metapelite protolith (Cesare *et al.*, 1997). As determined by SHRIMP U-Pb dating on zircon, the eruption age for El Hoyazo high-K calc-alkaline dacite is 6.33 ± 0.15 Ma (Zeck & Williams, 2002) whereas for Mazarrón dacite is 9.06 ± 0.53 Ma (Cesare *et al.*, 2003a). U-Pb age dating of zircon and monazite has also been performed on the restitic xenoliths enclosed in the lavas of El Hoyazo and Mazarrón in order to determine the age of anatexis. At El Hoyazo, Cesare *et al.* (2003a) found zircon overgrowths and monazite with melt inclusions providing an age of anatexis of 9.63 ± 0.26 Ma, *i.e.*, 3 Myr before the extrusion of the dacite. Conversely, at Mazarrón partial melting of the hosted crustal xenoliths was dated at 9.13 ± 0.18 Ma, coeval with the eruption age of the dacites. This means that

at El Hoyazo the magma resided in the crust, and the residuum of anatexis was kept at high-temperature for some 3 Myr, whereas at Mazarrón the magma residence time has been <0.8 Myr (considering the upper and lower 2σ limit of the age of melting and eruption, respectively). At El Hoyazo, most of the melt was syntectonically extracted from its source, and contaminated the ''external'' magma – the host-lava – which undoubtedly came from a different source (*e.g.*, Duggen *et al.*, 2005). The ''drops'' of melt that remained entrapped within the residual and newly-formed minerals of the xenoliths (see below) underwent a time- and temperature-dependent process of equilibration with the host-minerals. Regional anatectic events or magma chamber life-time of some 10^6 yrs are not unusual, the latter having been already documented in studies of the Long Valley volcanic system (Halliday *et al.*, 1989; Davies *et al.*, 1994).

3. Sample selection and analytical methods

One xenolith (HO50) and one lava (JOY6) from El Hoyazo, and four xenoliths (MAZ7, MAZ18, MAZ19, MAZ20) and one lava (MAZ12) from Mazarrón were collected and selected for this study. Xenolith HO50 has been previously characterized in many aspects including mineralogy and petrology (Cesare *et al.*, 2003b, 2005), petrophysics (Ferri *et al.*, 2007), and melt inclusion microstructures (Acosta *et al.*, 2007); the lava MAZ12 has been previously selected for geochronological work.

The samples were cut and split in two parts. The first was used to obtain thin sections for petrographic, SEM and Electron-microprobe analyses. The second was crushed and sieved to 500, 250, 160 μm, for mineral and whole rock chemical analyses. Enriched fractions of garnet, biotite, plagioclase, K-feldspar, and sillimanite + glass were obtained by a Frantz isodynamic separator and heavy liquids. Each separated fraction was handpicked under a binocular microscope to obtain >90 % purity. During handpicking we were also able to select and isolate single grains (<0.1 mg) of accessory phosphatic phases from MAZ7, MAZ19, and MAZ20. Only garnets with no visible inclusions were selected. After handpicking, the samples were repeatedly rinsed in deionised water and analytical grade acetone in ultrasonic bath to remove surface contamination. The biotite (250 μm) and garnet (250 μm and 500 μm) fractions were crushed in an agate mortar with acetone for exposing all the possible melt inclusions and then rinsed with milli-Q water. Variable amounts of garnet (50–300 mg) and biotite (70 mg) were weighed and leached to remove and analyse separately phosphatic inclusions. Garnet was leached in quartz-distilled 6N HCl at 80 °C for 1 ½ h (De Wolf *et al.*, 1996), whereas biotite was leached in cold quartz-distilled 1N HCl in ultrasonic bath for 2 h. The leached solutions were separated from the residue and centrifuged. Garnet residue, after rinsing with milli-Q water, was fused with an infrared laser beam CW Nd-YAG with 20W max power at the IGG-CNR of Pisa to obtain glass fragments that were dissolved in a HF-HNO$_3$-HCl mixture as for all the other separated fractions and whole-rock samples.

Trace element and radiogenic isotope analyses were performed, when possible, by splitting each dissolved sample in different aliquots. Trace element analyses were performed by ICP-MS at the University of Göttingen, whilst major elements on whole-rock samples were determined by XRF at the University of Florence following standard procedures. The single grains accessory phosphatic phases from MAZ7, MAZ19, and MAZ20 were analysed only for Sr and Nd isotopes.

Sr and Nd isotopes were measured in dynamic mode on a multiple collector Triton-Ti mass spectrometer at the Department of Earth Sciences of the University of Florence, following the procedures in Avanzinelli *et al.* (2005). Sr and Nd mass fractionation effects were corrected using an exponential law to $^{86}Sr/^{88}Sr = 0.1194$ and $^{146}Nd/^{144}Nd = 0.7219$, respectively. All errors reported are within run precision ($2\sigma_m$). Repeated analyses of SRM 987 and La Jolla standards yielded values of $^{87}Sr/^{86}Sr = 0.710249 \pm 9$ (2σ, $n = 14$), and $^{143}Nd/^{144}Nd = 0.511847 \pm 7$ (2σ, $n = 15$), respectively. Total procedural blank was <290 pg and <150 pg for Sr and Nd, respectively.

Representative samples of each mineral phase and glass were examined with a SEM to identify the inclusions. Analyses of mineral phases and glass from the xenoliths were performed on an electron microprobe JEOL JXA-8600 at the IGG-CNR in Florence. Laser ablation ICP-MS analyses on El Hoyazo sample were performed at the University of Perugia using a Thermo Electron X7 quadrupole equipped with Nd:YAG laser.

4. Results

4.1. Petrography

The El Hoyazo restitic xenolith (HO50) is a medium-grained foliated rock, which consists of garnet porphyroblasts (up to 0.5 cm in diameter) in a matrix constituted by plagioclase, biotite, fibrolitic sillimanite, graphite, ilmenite and rare cordierite in order of decreasing abundance. Garnet has generally euhedral shapes and may contain inclusions of sillimanite, monazite, zircon, biotite and glass. The xenolith contains abundant glass (quenched melt), both as inclusions in minerals and as intergranular films. Glass inclusions are ubiquitous in plagioclase and garnet (Fig. 2, details in Acosta *et al.*, 2007), whereas intergranular melt is often intergrown with fibrolitic sillimanite (Fig. 3, hereafter *Sil + gls;* mineral abbreviations after Kretz, 1983; *gls* = glass). The lava of El Hoyazo (JOY6) is described in detail by Zeck (1968): it consists largely of a glassy matrix with phenocrysts of cordierite, biotite and plagioclase, and xenocrysts of garnet, cordierite, spinel, sillimanite, and all the phases which derived from the disruption of the metapelitic xenoliths.

The four xenoliths from Mazarrón are very similar. They are fine- to medium-grained, weakly foliated hornfelses made of cordierite, fibrolitic sillimanite, plagioclase,
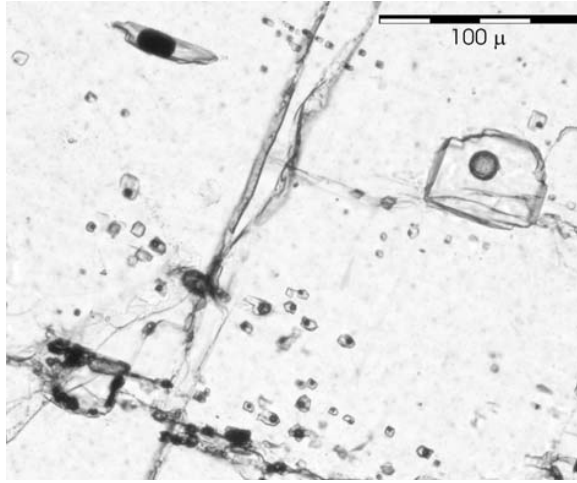
Fig. 2. Melt inclusions in plagioclase from sample HO50 from El Hoyazo. The shrinkage bubble within each inclusion is empty. Photomicrograph, transmitted plane polarised light. Width of view: 0.3 mm.

K-feldspar, biotite, garnet, hercynite (lacking in MAZ19), ilmenite, graphite, apatite, monazite and glass. No andalusite is observed in these Grt-bearing xenoliths. Like at El Hoyazo, melt inclusions are common in garnet and plagioclase, but here they occur also in cordierite. Biotite and garnet show evidence of resorption and replacement, in particular by cordierite (Fig. 4), which appears to grow (along with spinel) after a former *Grt-Bt-Sil*-melt assemblage. Plagioclase often shows a ''chessboard'' microstructure indicating two microstructural generations. Unlike at El Hoyazo, the abundant fibrolitic sillimanite is here intergrown with cordierite or feldspars (hereafter *Sil + Feld*), rather than with glass. In sample MAZ18 monazite is abundant and is observed as inclusion in cordierite, garnet and plagioclase, as well as in the matrix. As at El Hoyazo, the newly formed melt is preserved in all

the xenoliths as primary inclusions in garnet, biotite, feldspars, cordierite, ilmenite and phosphates.

4.2. Electron-microprobe analyses of minerals and glasses

Selected mineral and glass compositions from the studied samples are reported in Tables 1 and 2. Further microchemical data, including Fe^{2+}/Fe^{3+}, from sample HO50 are reported by Cesare *et al.* (2005) and Acosta-Vigil *et al.* (2007). In this rock, garnet is homogeneous with composition $Alm_{78}Prp_{18}Sps_2Grs_3$, plagioclase is an oligoclase-andesine (An_{29-32}) with minor Ca-richer crystals (An_{48}), biotite has high TiO_2 (≥ 5 wt. %) and $X_{Fe} = 0.66$–0.71, the rare cordierite has $X_{Fe} = 0.50$. The glass inclusions in garnet and plagioclase have a peraluminous rhyolitic composition (Table 2, see also Acosta-Vigil *et al.*, 2007).

At Mazarrón compositions are more variable, probably due to the more complex *P-T* history of the rocks (Álvarez-Valero *et al.*, 2007): compared with El Hoyazo, garnet is still rich in almandine (70–85 %), but has more Mn (up to 6 mol % spessartine) and may display a bell-shaped Mn growth zoning. Biotite shows a wide range of X_{Fe} (0.47–0.80), but is always Ti-rich. Cordierite is rich in Fe ($X_{Fe} = 0.58$–0.63), and hercynitic spinel has low Zn contents (<4 mol % gahnite) and $X_{Fe} = 0.80$. Plagioclase is more calcic and displays large variations (An_{39} to An_{86}), often related to a normal zoning. Similar zoning and compositional ranges are observed in plagioclase phenocrysts in the lava sample. Alkali-feldspar has an albite content of 15 to 19 mol %.

Glass inclusions represent high silica peraluminous liquids, with $SiO_2 > 70$ wt. % and alumina saturation index [molar $Al_2O_3/(K_2O + Na_2O + CaO)$] >1.2 (Table 2). In general, the glass of Mazarrón has alkali
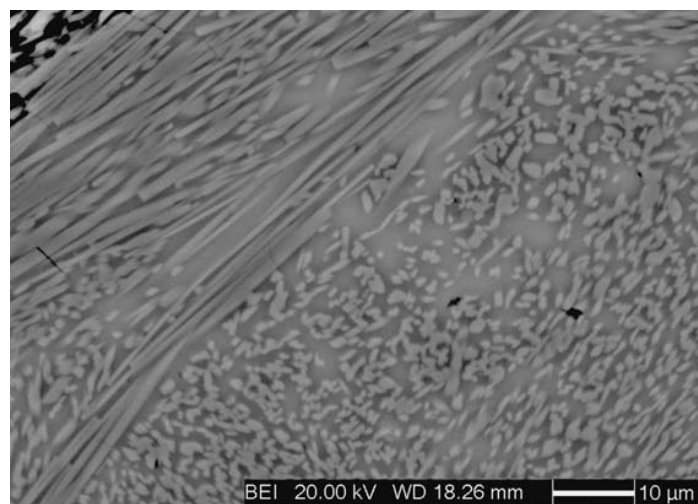

Fig. 3. Backscattered SEM image of an aggregate of acicular sillimanite (lighter gray) plus melt (darker gray) in sample HO50.
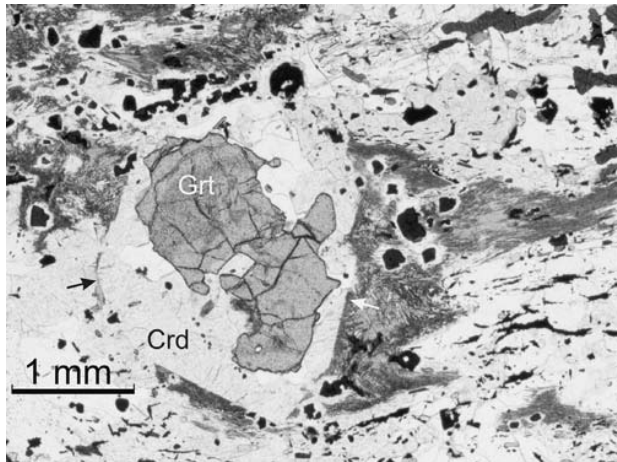
Fig. 4. Microstructure of garnet (Grt) replacement by cordierite (Crd) in sample MAZ7 from Mazarrón. The replacement takes place under static conditions, so that the trace of the original boundary of garnet is still visible (arrows). Photomicrograph, transmitted plan polarised light. Width of view: 5 mm.

content higher than El Hoyazo (Fig. 5; Table 2). Considering a simple two end-member mixing, the *Sil + gls* separates roughly consists of 20–30 % glass and 80–70 % sillimanite.

4.3. Major and trace element geochemistry

Major and trace element composition of host-lavas, mineral and glass separates and whole-rock xenoliths from El Hoyazo and Mazarrón are reported in Tables 3–5.

The LREE patterns of glass inclusions (*Sil + gls*), recalculated considering the presence of 70–80 % sillimanite, are more fractionated at Mazarrón than at El Hoyazo (Fig. 6a), resulting in lower Sm/Nd at Mazarrón than at El Hoyazo (Table 4). The trace element concentration of garnet and biotite HCl-leachates is referred to the initial weight of the host mineral, before leaching (Table 4). REE patterns (Fig. 6b) are similar in all HCl-leachates and do not resemble pure apatite or monazite patterns (*e.g.*, Bea *et al.*, 1994; Ayres & Harris, 1997). In fact, leachates have $(La/Sm)_N$ and $(Tb/Yb)_N$ in the range of 1.3–4.6 and 0.3–1.7, respectively (Table 4), suggesting that the accessory phosphatic phases removed during leaching consist of a mixture of mainly apatite $\pm$ monazite (*e.g.*, Bea *et al.*, 1994; Ayres & Harris, 1997). The shape of HREE pattern (Fig. 6b) could also indicate a minor contribution of xenotime (*e.g.*, Förster, 1998; Pyle *et al.*, 2001), which has been detected in the El Hoyazo xenoliths (Muñoz-Espadas *et al.*, 2000), to the accessory phosphate population. Minor contributions from the hosting mineral or melt inclusions to the HCl-leachates cannot be excluded considering other trace

Table 1. Average chemical compositions of minerals in xenoliths from El Hoyazo and Mazarrón.

	Biotite		Garnet		Plagioclase				K-feldspar	
	MAZ 7	MAZ 19	MAZ 7	HO 50	HO 50	HO 50	MAZ 18	MAZ 19	MAZ 7	MAZ 19
#	19	21	31	17	9	4	18	11	6	4
SiO$_2$	33.7	34.3	37.7	37.6	60.7	56.3	59.9	49.3	65.4	64.5
TiO$_2$	5.28	4.83	bdl	bdl	bdl	bdl	bdl	bdl	bdl	bdl
Al$_2$O$_3$	18.1	17.6	21.4	21.7	25.7	28.4	26.4	35.6	19.6	19.2
Cr$_2$O$_3$	0.09	0.08	bdl	bdl	nd	nd	nd	nd	nd	nd
Fe$_2$O$_3$				0.44	0.06	0.13	bdl	0.02	0.11	0.01
FeO	28.2	22.0	37.1	36.4	nd	nd	nd	nd	nd	nd
MnO	0.14	0.14	2.13	0.93	nd	nd	nd	nd	nd	nd
NiO	nd	nd	bdl	bdl	nd	nd	nd	nd	nd	nd
MgO	3.99	8.74	2.23	3.37	nd	nd	nd	nd	nd	nd
CaO	0.04	bdl	1.07	1.03	6.15	9.11	7.82	12.79	0.22	0.12
Na$_2$O	0.34	0.36	bdl	bdl	7.62	5.15	6.28	2.94	2.02	1.74
K$_2$O	8.24	9.21	bdl	bdl	0.83	0.56	0.78	0.17	12.4	14.8
SrO	nd	nd	nd	nd	0.19	0.19	nd	nd	0.23	nd
BaO	0.15	0.28	nd	nd	0.02	0.04	nd	nd	0.37	nd
F	0.27	0.18	nd	nd	nd	nd	nd	nd	nd	nd
Cl	0.88	0.63	nd	nd	nd	nd	nd	nd	nd	nd
Sum	99.4	98.4								
F + Cl = O	0.32	0.22								
Sum	99.1	98.1	101.6	101.5	101.2	99.8	101.3	100.8	100.4	100.3
Mg#	0.20	0.41								
Prp			9	18						
Sps			5	2						
Grs			3	3						
Alm			83	78						
Ab					66	49	57	29	19	15
An					29	48	39	70	1	1
Or					5	3	5	1	79	84

= number of analyses averaged; nd = not determined; bdl = below detection limit. Other chemical data are available upon request.

Table 2. Selected electron-microprobe analyses of *sil* + *gls* and glass inclusions from El Hoyazo and Mazarrón xenoliths.

#	HO50 13 $Sil + gls$	HO50 23 $Sil + gls$	HO50 27 $Sil + gls$	HO50 7 incl in Grt	MAZ18 1 $Sil + gls$	MAZ18 2 $Sil + gls$	MAZ19 3 incl. in Ilm	MAZ19 5 incl in Cord	MAZ20 3 incl. in Ilm	MAZ7 4 incl. in Grt	MAZ7 5 incl. in Ilm	MAZ7 6 incl. in Ilm	MAZ7 8 incl. in Spin
SiO_2	49.7	41.8	47.4	72.6	39.4	43.3	72.9	73.7	71.4	71.3	74.0	73.8	71.1
TiO_2	0.09	0.03	0.04	0.1	0.0	0.0	0.65	0.09	0.53	0.13	0.68	0.62	0.19
Al_2O_3	44.6	57.0	48.9	14.7	61.8	55.9	15.0	13.8	15.4	14.5	14.6	15.0	15.0
FeO	0.86	0.67	0.78	1.96	0.44	0.45	2.46	2.05	2.41	2.09	2.02	1.88	1.69
MnO	0.0	0.03	0.0	0.0	0.0	0.0	0.0	0.15	0.08	0.1	0.02	0.13	0.11
MgO	0.10	0.04	0.07	0.09	0.09	0.02	0.09	0.05	0.05	0.0	0.03	0.0	0.06
CaO	0.30	0.12	0.22	0.66	0.07	0.15	0.88	0.66	0.84	0.53	0.68	0.77	0.94
Na_2O	1.01	0.36	0.64	2.22	0.05	0.33	1.82	1.48	2.45	2.2	2.17	2.66	1.77
K_2O	2.05	0.78	1.54	3.75	0.14	0.77	6.00	5.9	6.33	6.15	5.25	6.09	6.64
P_2O_5	0.18	0.04	0.0	0.32	0.0	0.09	0.19	0.23	0.21	0.3	0.31	0.2	0.16
SrO	0.02	nd	0.03	0.05	nd	nd	nd	nd	nd	nd	nd	nd	nd
BaO	0.04	nd	0.03	0.02	nd	nd	nd	nd	nd	nd	nd	nd	nd
F	nd	0.11	0.17	nd	nd	bdl	bdl	0.25	0.2	0.11	bdl	0.16	bdl
Cl	nd	bdl	bdl	nd	nd	0.03	0.36	0.47	0.42	0.45	0.04	0.16	0.37
ASI				1.65			1.36	1.38	1.24	1.29	1.39	1.22	1.27
Sum	98.9	100.9	99.7	96.6	102.0	101.0	100.0	98.1	99.7	97.3	99.7	101.1	97.7

Symbols for minerals after Kretz (1983); # = number of analyses averaged; incl. = inclusion; nd = not determined, bdl = below detection limit, ASI = Alumina Saturation Index.
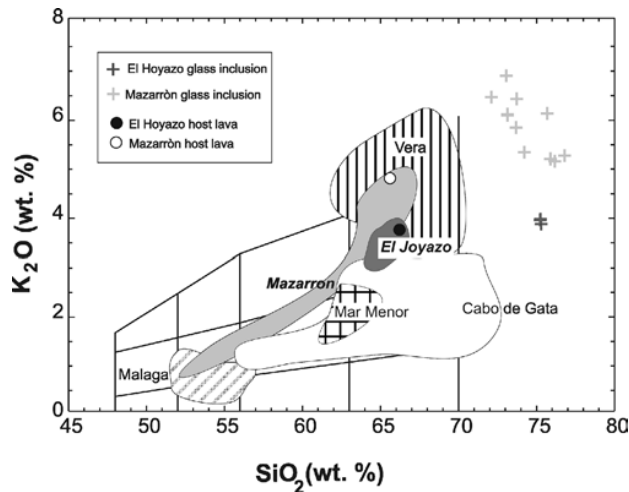
Fig. 5. K₂O (wt. %) *versus* SiO₂ (wt. %) classification diagram (Peccerillo & Taylor, 1976) of the Neogene volcanic rocks from SE Spain. Source of data: Munksgaard, 1985; Benito *et al.*, 1999; Turner *et al.*, 1999; Zeck *et al.*, 1999; Muñoz-Espadas *et al.*, 2000; Duggen *et al.*, 2004. Chemical composition of glass inclusions in mineral phases from El Hoyazo and Mazarrón xenoliths are also reported.

Table 3. Whole-rock major element composition (wt %) of metapelitic xenoliths and host-lavas.

	HO50 xenolith	JOY6 lava	MAZ18 xenolith	MAZ12 lava
SiO_2	47.5	62.8	52.7	63.6
TiO_2	2.11	0.76	1.49	0.71
Al_2O_3	25.0	17.2	23.2	15.7
FeO	6.73	4.97	8.06	4.24
Fe_2O_3	2.82	0.67	0.63	0.83
MnO	0.05	0.08	0.12	0.08
MgO	2.36	1.27	1.88	2.16
CaO	2.93	2.35	1.4	2.57
Na_2O	2.87	1.46	1.48	2.24
K_2O	4.4	3.71	7.24	4.47
P_2O_5	0.05	0.14	0.14	0.32
LOI	3.24	3.47	1.67	3.08
Total	100.0	98.9	100.0	100.0

element characteristics. In particular, Rb/Sr is uncommonly high in all HCl-leachates for phosphates (*e.g.*, Prowatke & Klemme, 2006; Table 4) and Eu anomaly is positive in biotite leachates from El Hoyazo, which, again, is not typical of apatite, monazite or xenotime (Bea *et al.*, 1994; Ayres & Harris, 1997; Förster, 1998).

The ICP-MS REE data of garnet separates yield Sm/Nd < 0.5 (Table 4; Fig. 6c), which is not typical of almandine-pyrope garnets from similar rocks (DeWolf *et al.*, 1996 and reference therein). By contrast, garnet data obtained by LA-ICP-MS have the expected Sm/Nd > 1 (Fig. 6c; Table 5), suggesting both a possible contribution of melt inclusions to the LREE budget of garnet separates and only partial removal of LREE-enriched phosphatic inclusions

during the leaching procedure (*e.g.*, Anczkiewicz & Thirlwall, 2003; Jung & Mezger, 2003).

4.4. Sr and Nd isotope geochemistry

Sr and Nd isotope data have been determined on host-lavas, whole-rock and mineral separates (including the *Sil + gls* and *Sil + Feld* separates, and the single grains phosphatic inclusions) of the xenoliths (Table 6). In general, the internal precision of Sr and Nd isotope measurements was excellent for all the samples (~10 ppm), with the exception of Nd isotope measurements of HCl-leachates and the glass separate from El Hoyazo because of a poor signal during measurement. These samples will then be considered only for their Sr isotope composition. The Sr and Nd isotope composition of the single grains phosphatic inclusions from Mazarrón cannot be corrected to the initial value because we did not analyse the concentration of the parent-daughter elements. The relatively young age (~9 Ma) of the samples along with the likely parent-daughter ratios (Fig. 6b and Bea *et al.*, 1994; Ayres & Harris, 1997; Förster, 1998) implies that the measured and initial isotopic ratios cannot be much different and do not invalidate the results.

Despite the significant re-crystallisation in both suites of xenoliths, the initial isotopic compositions of the Mazarrón samples exhibit a marked disequilibrium in comparison with the quasi-equilibrium of the samples of El Hoyazo (Table 6). This is not surprising given the longer residence time of the magma at El Hoyazo than Mazarrón. The most peculiar feature is, however, that the HCl-leachates from both El Hoyazo and Mazarrón have a relatively ''unradiogenic'' Sr isotope composition (0.710–0.713, Table 6) in comparison with other mineral phases. This is consistent with the Sr isotope composition of the single grains phosphatic inclusions and provide evidence, along with REE patterns (Fig. 6b), that the leaching procedure has mainly removed phosphates from the host-minerals.

5. Discussion

Studies on migmatites (Barbero *et al.*, 1995; Tommasini & Davies, 1997; Zeng *et al.*, 2005a and b and references therein) and experimental data simulating crustal anatexis (Knesel & Davidson, 2002 and references therein) have raised the idea that during high-temperature events, such as high-grade metamorphism and partial melting, rock-forming minerals do not necessarily attain isotope equilibrium. Thus, the Sr and Nd isotope signature of crustal melts can be determined by the proportions of each mineral phase entering the melt (*i.e.*, non modal melting). Rb-Sr systematics of anatectic melts is strongly controlled by the muscovite-biotite *versus* plagioclase-K-feldspar ratio entering the melt. On the other hand, accessory phases, such as apatite and monazite, might play a critical role in controlling the Nd isotope composition of anatectic melts (Zeng *et al.*, 2005a and c).

Table 4. Trace element (ppm, ICP-MS) compositions of whole-rock and separated phases from metapelitic xenoliths and host-lavas.

	HO50 whole-rock	HO50 *Sil + gls*	HO50 *Bt*	HO50 *Pl*	HO50 *Grt*	HO50 *250* μm *Grt* leach.	HO50 *500* μm *Grt* leach.	HO50 *Bt* leach.
Sc	13.6	2.31	43.9	bdl	243	0.94	0.18	10.4
V	139	84.9	541	6.67	48.5	0.31	0.95	94.1
Co	12.7	1.42	73.6	1.00	27.5	0.12	0.14	11.3
Ni	26.4	4.42	139	3.14	1.62	0.07	0.41	20.9
Ba	640	241	1357	145	1.39	0.64	1.97	248
Rb	102	83.3	346	7.96	0.57	0.06	0.37	70.6
Sr	497	92.8	15.6	1153	2.48	0.17	0.54	6.54
Zr	7.32	10.7	5.5	1.44	73.0	0.07	0.14	0.85
Y	15.9	6.43	0.30	3.75	346	1.47	0.71	0.12
Nb	19.1	4.72	60.7	0.74	0.30	0.01	0.21	1.07
Hf	0.36	0.52	0.25	0.08	2.20	bdl	0.02	0.04
Ta	2.87	0.49	6.07	0.20	0.22	bdl	bdl	nd
Pb	48.8	9.7	14.4	85.7	0.18	0.13	bdl	3.20
Th	18.0	1.50	0.87	11.0	2.29	0.11	0.11	0.02
U	3.42	1.73	0.18	1.84	0.45	0.02	0.03	0.02
Rare Earth Elements								
La	51.2	3.32	2.62	32.1	6.59	0.33	0.19	0.22
Ce	108	5.22	5.11	67.5	13.8	0.78	0.28	0.20
Pr	12.5	0.72	0.61	7.82	1.57	0.08	0.04	0.03
Nd	46.3	2.62	2.22	28.6	6.02	0.29	0.14	0.09
Sm	8.47	0.73	0.43	5.45	1.61	0.06	0.04	0.03
Eu	5.16	0.77	0.81	10.9	0.20	0.01	0.01	0.17
Gd	6.94	0.96	0.33	3.89	5.83	0.07	0.07	0.03
Tb	0.79	0.21	0.04	0.40	2.97	0.02	0.01	0.01
Dy	4.49	1.26	0.14	1.63	43.2	0.20	0.11	0.04
Ho	0.76	0.19	0.02	0.19	13.8	0.06	0.03	0.01
Er	2.06	0.51	0.06	0.37	47.5	0.20	0.08	bdl
Tm	0.31	0.08	Bdl	0.04	8.48	0.04	0.01	bdl
Yb	2.10	0.40	Bdl	0.17	52.1	0.22	0.09	bdl
Lu	0.35	0.09	Bdl	0.02	9.29	0.04	0.02	bdl
Eu/Eu*	2.06	2.79	6.50	7.25	0.20	0.47	0.56	17.3
(La/Sm)$_N$	3.80	2.86	3.79	3.70	2.57	3.46	2.86	4.61
(Tb/Yb)$_N$	1.65	2.28		9.99	0.25	0.40	0.69	

	JOY6 lava	MAZ18 whole-rock	MAZ19 *Sil + gls/ Sil + feld*	MAZ19 *Pl*	MAZ19 *Kfs*	MAZ19 *Bt*	MAZ19 *Grt* leach.	MAZ19 *Bt* leach.
Sc	15.3	25.9	1.94	1.40	0.039	118	1.08	0.79
V	94.9	207	161	127	2.65	947	1.15	10.5
Co	11.4	17.4	3.05	0.70	0.16	66.8	0.20	0.90
Ni	23.3	37.9	52.2	13.7	1.16	136	2.16	1.79
Ba	462	2276	725	566	6383	1756	9.98	75.8
Rb	132	176	21.6	7.26	239	540	0.62	7.84
Sr	264	507	742	1416	1520	50.0	2.65	6.21
Zr	43.7	4.32	4.37	0.91	0.30	6.48	0.01	bdl
Y	20.7	21.2	8.53	4.78	1.36	6.21	1.66	0.29
Nb	11.5	20.8	2.67	0.85	0.25	94	0.15	0.10
Hf	1.61	0.22	0.10	0.023	0.010	0.39	Bdl	bdl
Ta	1.11	2.00	0.14	0.10	0.039	5.35	0.014	bdl
Pb	26.1	103	43.3	53.1	171	19.6	0.30	4.4
Th	21.3	20.6	10.0	1.15	1.37	10.9	0.04	bdl
U	5.67	4.21	4.29	0.85	0.30	1.45	0.08	0.14
Rare Earth Elements								
La	46.5	65.5	29.7	16.0	7.54	34.0	0.58	0.20
Ce	92.2	135	60.3	29.6	12.9	68.9	1.22	0.48
Pr	10.2	15.6	7.41	3.37	1.42	8.39	0.14	0.06
Nd	36.6	57.9	28.8	12.3	5.28	32.3	0.54	0.30
Sm	6.58	10.9	5.27	2.17	0.95	5.71	0.10	0.07
Eu	1.39	4.02	2.82	5.00	7.20	0.90	0.006	0.002
Gd	5.90	9.61	3.57	1.41	0.70	4.39	0.08	0.03

Table 4.   Continued

	JOY6	MAZ18	MAZ19	MAZ19	MAZ19	MAZ19	MAZ19	MAZ19
		whole-	*Sil + gls/*					
	lava	rock	*Sil + feld*	*Pl*	*Kfs*	*Bt*	*Grt* leach.	*Bt* leach.
Tb	0.79	1.20	0.42	0.18	0.07	0.47	0.02	0.005
Dy	4.36	5.97	1.97	0.93	0.34	1.91	0.22	0.05
Ho	0.78	0.94	0.31	0.16	0.05	0.25	0.07	0.01
Er	2.22	2.44	0.59	0.35	0.08	0.35	0.25	0.02
Tm	0.32	0.32	0.08	0.04	bdl	0.05	0.04	0.002
Yb	2.02	2.03	0.51	0.28	0.07	0.29	0.31	0.03
Lu	0.29	0.29	0.07	0.04	0.01	0.05	0.05	0.003
Eu/Eu*	0.68	1.20	1.99	8.74	27.13	0.55	0.21	0.11
(La/Sm)$_N$	4.45	3.77	3.55	4.62	5.02	3.75	3.68	1.78
(Tb/Yb)$_N$	1.72	2.61	3.67	2.78	4.83	7.24	0.27	0.85

	MAZ20	MAZ20	MAZ20	MAZ20	MAZ20	MAZ20	MAZ7	MAZ7
	Sil + gls/				*Grt*		*Sil + gls/*	
	Sil + feld	*Kfs*	*Bt*	*Grt*	leach.	*Bt* leach.	*Sil + Feld*	*Kfs*
Sc	2.54	0.49	112	472	0.18	1.28	3.86	0.86
V	8.52	6.34	796	99.4	1.01	13.0	17.2	10.5
Co	1.56	0.52	71.4	34.7	0.07	1.35	4.83	2.36
Ni	7.70	4.07	160	1.89	0.04	3.0	26.4	7.83
Ba	312	234	3025	14.6	11.3	69.0	487	2022
Rb	151	8.28	544	1.17	0.22	11.4	95.7	197
Sr	715	1958	36.4	13.9	1.09	4.32	1455	1083
Zr	15.7	1.08	7.01	66.2	bdl	bdl	20.4	1.23
Y	13.0	13.8	9.4	1228	1.29	1.29	11.1	10.3
Nb	4.64	0.97	88	0.68	0.06	0.18	3.09	1.05
Hf	0.89	0.05	0.44	2.49	bdl	bdl	1.08	0.09
Ta	0.80	0.18	5.21	0.14	bdl	bdl	0.52	0.18
Pb	76	74	16.7	0.74	0.22	1.22	58	198
Th	15.4	21.3	18.0	4.47	bdl	bdl	17.8	6.57
U	13.8	2.43	1.87	1.23	0.09	0.26	5.36	1.52
Rare Earth Elements								
La	21.7	61.7	48.3	13.9	0.24	0.63	40.6	29.3
Ce	43.6	122	99.6	28.2	0.57	1.69	79.4	55.0
Pr	5.31	14.2	12.0	3.38	0.07	0.25	9.53	6.53
Nd	20.6	54.4	46.5	13.5	0.31	1.16	36.8	24.7
Sm	4.06	9.56	8.17	3.82	0.08	0.31	6.44	4.58
Eu	2.95	8.03	1.13	0.64	bdl	0.01	5.06	6.93
Gd	2.93	6.72	6.24	15.3	0.07	0.24	4.31	3.64
Tb	0.41	0.79	0.68	8.29	0.02	0.04	0.48	0.47
Dy	2.35	3.60	2.92	123	0.19	0.24	2.38	2.41
Ho	0.43	0.51	0.37	42	0.05	0.05	0.39	0.38
Er	1.15	0.79	0.42	166	0.15	0.11	0.81	0.76
Tm	0.17	0.08	0.04	27.6	0.02	0.02	0.11	0.08
Yb	1.19	0.42	0.18	194	0.17	0.10	0.69	0.48
Lu	0.18	0.05	0.03	29.0	0.03	0.01	0.09	0.06
Eu/Eu*	2.61	3.06	0.48	0.25	0.00	0.16	2.94	5.19
(La/Sm)$_N$	3.36	4.06	3.72	2.29	1.96	1.28	3.97	4.02
(Tb/Yb)$_N$	1.53	8.40	16.50	0.19	0.46	1.67	3.10	4.32

	MAZ7	MAZ7	MAZ7	MAZ7	MAZ7	MAZ12
				Grt	*Bt*	
	Pl	*Bt*	*Grt*	leach.	leach.	lava
Sc	3.26	168	375	0.25	2.33	14.4
V	93.6	1573	88.4	0.90	26.4	81.4
Co	2.09	95.7	26.2	0.32	5.67	9.99
Ni	12.1	259	1.54	0.94	9.82	24.1
Ba	422	1843	3.90	2.81	70.9	1023
Rb	47.2	459	0.80	0.16	9.88	208
Sr	1272	44.9	1.16	bdl	12.2	420
Zr	2.47	8.48	18.9	bdl	bdl	51.4

Table 4.   Continued

	MAZ7	MAZ7	MAZ7	MAZ7 Grt leach.	MAZ7 Bt leach.	MAZ12 lava
	Pl	*Bt*	*Grt*			
Y	8.40	4.81	697	0.61	2.06	19.2
Nb	1.24	84.9	0.88	0.01	0.17	15.7
Hf	0.13	0.55	0.70	bdl	0.002	1.87
Ta	0.21	4.70	0.004	bdl	bdl	2.19
Pb	79	29.4	0.47	0.51	4.86	74
Th	9.71	8.11	0.74	bdl	bdl	39.7
U	1.63	1.48	0.39	0.04	0.32	12.7
Rare Earth Elements						
La	30.5	22.0	2.33	0.05	0.67	45.1
Ce	56.8	43.8	4.77	0.14	1.94	95.4
Pr	6.63	5.32	0.58	0.01	0.25	11.6
Nd	25.0	20.3	2.51	0.07	1.18	44.6
Sm	4.30	3.61	1.35	0.02	0.33	8.49
Eu	5.88	0.75	0.21	bdl	0.02	1.81
Gd	3.03	2.83	8.82	0.01	0.30	6.80
Tb	0.37	0.31	5.19	0.01	0.06	0.87
Dy	1.91	1.35	76.6	0.08	0.41	4.53
Ho	0.31	0.19	25.6	0.02	0.08	0.74
Er	0.64	0.31	97.2	0.07	0.20	2.02
Tm	0.08	0.04	16.5	0.01	0.03	0.28
Yb	0.48	0.29	118	0.09	0.15	1.74
Lu	0.07	0.05	17.3	0.01	0.02	0.25
Eu/Eu*	4.99	0.71	0.19		0.14	0.73
$(La/Sm)_N$	4.46	3.84	1.09	1.44	1.28	3.34
$(Tb/Yb)_N$	3.38	4.66	0.19	0.26	1.68	2.21

leach. = Grt and Bt leachates, symbols for minerals after Kretz (1983); bdl = below detection limit.

Table 5. LA-ICP-MS data of garnet from El Hoyazo and Mazarrón xenoliths.

Mineral	HO 50 Grt	HO 50 Grt	HO 50 Grt	HO 50 Grt	HO 50 Grt	HO 50 Grt	HO 50 Grt	HO 50 Grt	HO 50 Grt
La	bdl	bdl	bdl	bdl	bdl	bdl	bdl	0.09	bdl
Ce	bdl	bdl	bdl	bdl	bdl	bdl	bdl	bdl	bdl
Pr	bdl	bdl	bdl	bdl	bdl	bdl	bdl	bdl	bdl
Nd	0.09	0.08	bdl	0.12	0.10	0.41	bdl	bdl	bdl
Sm	0.41	0.56	0.40	0.41	0.33	bdl	0.85	0.56	0.58
Eu	0.09	0.06	0.08	0.08	0.08	0.11	0.14	0.19	0.15
Gd	5.37	5.72	4.52	4.74	4.21	5.27	6.34	5.34	6.58
Tb	3.30	3.68	2.96	3.05	2.71	3.25	3.63	3.22	4.60
Dy	60.7	67.0	49.6	51.0	48.3	48.8	45.9	46.8	75.6
Ho	23.0	24.7	17.2	19.5	16.2	17.7	11.3	12.3	27.9
Er	86.9	92.3	65.3	86.5	62.8	67.6	35.5	43.4	102
Tm	14.2	15.4	11.5	16.8	10.9	12.9	5.77	7.10	15.2
Yb	98.5	113	91.0	143	79.5	99.0	42.1	56.0	101
Lu	13.7	15.8	13.8	24.8	12.0	15.3	6.05	8.24	14.0
Sm/Nd	4.39	6.94		3.47	3.46				

Symbols for minerals after Kretz (1983); bdl = below detection limit.

Partial melting of El Hoyazo and Mazarrón xenoliths is testified by primary melt inclusions occurring in all mineral phases of the xenoliths, by thin intergranular films of glass and by sillimanite intergrown with glass, the last characteristic being more pronounced at El Hoyazo. Thermobarometric estimates as well as phase compositions and reaction textures indicate that the degree of partial melting in the xenoliths of Mazarrón is greater than in those of El Hoyazo (Álvarez-Valero, 2004). In particular, the xenoliths of Mazarrón evolve from the typical assemblage at El Hoyazo (*Grt-Bt-Sil-Pl*-melt), through further melting of garnet, biotite and sillimanite
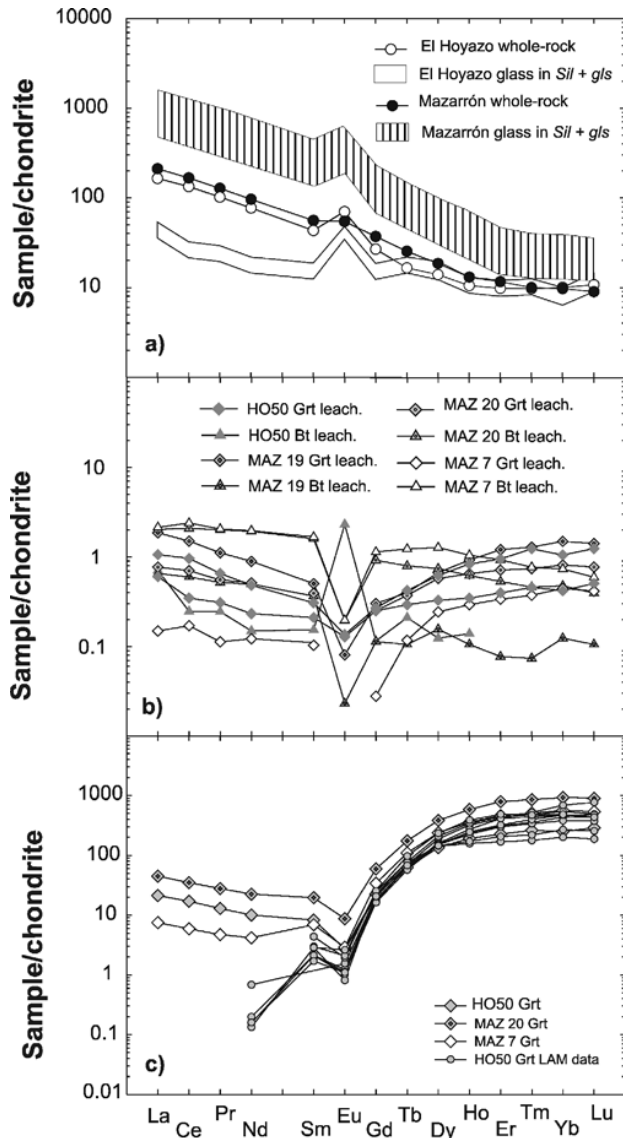
Fig. 6. Chondrite normalised patterns of Rare Earth Elements for (a) glasses in *Sil + gls* fractions, (b) biotite and garnet leachates and (c) garnet from El Hoyazo and Mazarrón xenoliths, including LAM data for garnet in the El Hoyazo sample. The range of REE composition of glasses has been recalculated considering that the *Sil + gls* fraction consists of 20–30 % glass and 80–70 % sillimanite. Normalising values are from Boynton (1984).

to produce peritectic cordierite, K-feldspar, more calcic plagioclase and spinel. Indeed, fibrolitic sillimanite in Mazarrón samples is often intergrown with newly formed feldspars (*i.e.*, *Sil + Feld*), which are likely to be in isotopic equilibrium with the melt.

In addition to the extensive re-crystallisation experienced by the xenoliths, the assessment of isotopic homogenisation prior to the onset of melting is complicated by their entrapment within the host-lavas which have a different isotopic signature (Table 6) and could have interacted with them. In Fig. 7 we show the initial Sr-Nd isotope

composition of all analysed samples. Excluding the HCl-leachates and the single grains phosphates, it is clear that the major mineral and glass phases at El Hoyazo exhibit a quasi-equilibrium condition, whilst the most marked disequilibrium observed at Mazarrón could be due to isotopic exchange between the host-lava and the xenoliths (MAZ 12 and MAZ 18, Fig. 7). Although we cannot totally exclude this possibility, there are some lines of evidence that question this hypothesis: (i) the whole rock isotopic compositon of the Mazarrón xenolith (MAZ 18, Table 6) does not necessarily correspond to the isotopic composition of the other Mazarrón xenoliths from which we analysed the mineral and glass phases; (ii) it is unclear why the mineral and glass phases of the El Hoyazo xenolith, which had a longer residence time at melting temperatures (~3 Myr), do not exhibit any significant isotopic exchange with the host-lava (JOY 6, Fig. 7), despite the more extreme isotopic difference in comparison with Mazarrón; (iii) the HCl-leachates and the single grains phosphatic inclusions have a Sr isotope composition that is not consistent with any exchange between the xenoliths and the host-lavas (Fig. 7).

Although the available data do not permit a detailed and conclusive assessment, the completely different radiogenic isotope signature of HCl-leachates and single grains phosphatic inclusions indicates that the accessory phases enclosed in garnet and biotite did not attain isotopic equilibrium during the high-grade temperature event, and this can explain the Sr-Nd isotope characteristics of the other mineral and glass phases. Their not complete removal during the leaching procedure (*e.g.*, Fig. 6c and Anczkiewicz & Thirlwall, 2003; Jung & Mezger, 2003) can account for the small, although detectable, disequilibrium observed in the leached garnet and biotite (Fig. 7); equally, their contribution to the Sr and Nd budget of the melt can explain its isotopic composition along with that of the newly formed and residual feldspars.

The ~3 Myr residence time of the magma at El Hoyazo has then determined the attainment of quasi-equilibrium isotopic conditions among the glass and mineral phases (except accessory phosphatic phases), whilst the shorter magma residence time at Mazarrón has favoured the preservation of the observed Sr-Nd isotope disequilibrium (Fig. 7). In fact, given the very different parent-daughter ratios of, for example, plagioclase and biotite (Rb-Sr systematics), along with garnet and other minerals (Sm-Nd systematics), the relative isotopic homogeneity of the xenolith-forming minerals at El Hoyazo would be unsustainable unless the high-temperature (>800 °C) regime were maintained for 10^6 yrs timescales, allowing mineral to reset their isotopic composition.

The isotopic disequilibrium, particularly Sr isotopes (Fig. 7), observed in the accessory phosphate inclusions can be related to the armouring effect of the host minerals. Element transport between different mineral phases is controlled by the mineral in which diffusion is the slowest (Gilletti, 1991), and a study by Burton *et al.* (1995) confirmed the importance of adjacent phases and the relative

Table 6. Sr and Nd isotope data of whole-rock and separated phases from El Hoyazo and Mazarrón xenoliths.

	$^{87}Rb/^{86}Sr$	$^{87}Sr/^{86}Sr_m$	$^{87}Sr/^{86}Sr_i$	$^{147}Sm/^{144}Nd$	$^{143}Nd/^{144}Nd_m$	$^{143}Nd/^{144}Nd_i$
Host-lava						
JOY6	1.44	0.714345 ± 6	0.71421	0.109	0.512137 ± 9	0.51213
MAZ12	1.44	0.716320 ± 7	0.71614	0.115	0.512077 ± 4	0.51207
Xenolith – El Hoyazo						
HO50 wr	0.593	0.730962 ± 7	0.73091	0.111	0.512008 ± 4	0.51200
HO50 gls	2.60	0.730012 ± 9	0.72978	0.169	0.512018 ± 12	0.51201
HO50 Bt	64.4	0.735076 ± 7	0.72922	0.119	0.512008 ± 5	0.51201
HO50 Pl	0.020	0.731363 ± 7	0.73136	0.115	0.512016 ± 6	0.51202
HO50 Grt	0.671	0.730902 ± 7	0.73084	0.162	0.512013 ± 7	0.51201
HO50 GrtL (250 μm)	1.02	0.713571 ± 6	0.71348	0.125	0.512015 ± 9	0.51202
HO50 GrtL (500 μm)	1.96	0.713063 ± 8	0.71288	0.178	0.512036 ± 12	0.51203
Xenolith – Mazarrón						
MAZ18 wr	1.00	0.721266 ± 7	0.72114	0.114	0.512003 ± 4	0.51200
MAZ7 gls	0.191	0.716538 ± 6	0.71651	0.106	0.512055 ± 6	0.51205
MAZ7 Kfs	0.528	0.722111 ± 7	0.72204	0.112	0.512012 ± 5	0.51200
MAZ7 Pl	0.108	0.719039 ± 8	0.71903	0.104	0.512044 ± 5	0.51204
MAZ7 Bt	29.6	0.723287 ± 9	0.71950			
MAZ7 Grt	1.99	0.720833 ± 8	0.72058	0.324	0.512022 ± 6	0.51200
MAZ7 GrtL	0.0839	0.710370 ± 8	0.71036			
MAZ7 BtL	2.35	0.711271 ± 8	0.71097	0.167	0.512038 ± 7	0.51203
MAZ19 gls	0.084	0.717065 ± 7	0.71705	0.111	0.512044 ± 4	0.51204
MAZ19 Pl	0.0148	0.717656 ± 8	0.71765	0.107	0.512059 ± 6	0.51205
MAZ19 Kfs	0.456	0.717981 ± 7	0.71792	0.108	0.512024 ± 6	0.51202
MAZ19 Bt	31.3	0.720468 ± 8	0.71647	0.107	0.512012 ± 4	0.51201
MAZ19 Grt		0.718730 ± 7			0.512005 ± 4	
MAZ19 GrtL	0.681	0.711396 ± 8	0.71131	0.111	0.512033 ± 11	0.51203
MAZ19 BtL	3.65	0.710784 ± 7	0.71032	0.145	0.512058 ± 26	0.51205
MAZ20 gls	0.612	0.718008 ± 8	0.71793	0.119	0.512060 ± 5	0.51205
MAZ20 Kfs	0.0122	0.717940 ± 7	0.71794	0.106	0.512036 ± 5	0.51203
MAZ20 Bt	43.3	0.722734 ± 8	0.71720	0.106	0.512019 ± 5	0.51201
MAZ20 Grt	0.244	0.718121 ± 9	0.71809	0.171	0.512017 ± 5	0.51201
MAZ20 GrtL	0.580	0.711411 ± 9	0.71134	0.151	0.512047 ± 44	0.51204
MAZ20 BtL	7.65	0.712382 ± 7	0.71140	0.161	0.512076 ± 7	0.51207
Single grains						
MAZ7 Phos		0.711960 ± 8			0.512008 ± 4	
MAZ19 Phos		0.713231 ± 7			0.512060 ± 5	
MAZ20 Phos		0.711172 ± 8			0.512063 ± 5	

wr = whole-rock, gls = $Sil + gls$ fraction, GrtL and BtL = Grt and Bt leachates respectively, Phos = single grains accessory phosphatic phases (see text); symbols for minerals after Kretz (1983); errors in measured isotopic ratios refer to the last significant digits and represent $\pm 2\sigma_m$ internal precision.

diffusion rate for element and isotope homogenisation. Elemental diffusion profiles in phosphates enclosed within garnet and biotite can be modelled considering a composite medium with a resistance at the interface (Equations 3.49 and 3.50, Crank, 1975). The results indicate that chemical homogenisation is much slower than in homogeneous media. The diffusion coefficient (D) for Sr in garnet at the temperature of the thermal event in SE Spain (~850 °C) is ~10^{-18} cm^2/s (Burton et al., 1995), whereas that in apatite is ~10^{-16} cm^2/s (Cherniak & Ryerson, 1993). The lack of isotopic equilibrium can thus be the result of a slow diffusion of Sr between the inclusions and the hosting minerals. This, however, cannot be the only explanation because biotite, as opposed to garnet, has a relatively fast Sr diffusion coefficient at subsolidus temperature (Giletti, 1991; Burton et al., 1995). In both minerals, however, Sr is not easily accepted into their lattices as suggested by the $\ll 1$ crystal partition coefficient (Kd^{Sr}) of biotite and garnet (e.g., Bea et al., 1994). Thus, biotite and garnet constitute a

chemical barrier for the movement of Sr during diffusion. This means that Sr remobilisation in response to the thermal event did not affect the phosphatic inclusions within garnet and biotite, which retained a relatively unradiogenic Sr isotope signature.

Similar arguments (slow diffusion and $Kd^{Nd} < 1$) can be claimed for the Nd isotope disequilibrium observed in the accessory phosphate inclusions (Fig. 7), although the extent of disequilibrium is less marked than for Sr isotopes. The reason could be twofold: (i) the accessory phosphate inclusions did not have enough time, since their growth and/or last resetting event, to develop different Nd isotope compositions owing to the less marked parent-daughter ratio difference among rock-forming minerals than the Rb-Sr system, along with the slower decay constant of ^{147}Sm than ^{87}Rb; (ii) the accessory phosphate inclusions are a mixture of apatite $\pm$ monazite $\pm$ xenotime: apatite (and xenotime) and monazite have lower and higher Sm/Nd, respectively, than
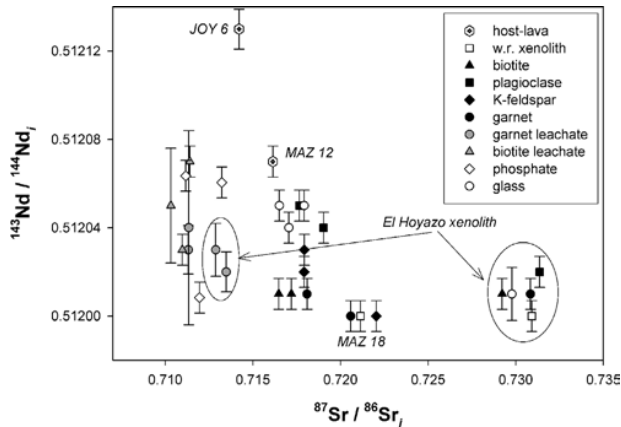
Fig. 7. Age-corrected $^{87}Sr/^{86}Sr_i$ *versus* $^{143}Nd/^{144}Nd_i$ of whole-rock and separated phases from El Hoyazo and Mazarrón xenoliths. Eruption age is 6.3 Ma and of 9.1 Ma for the El Hoyazo and Mazarrón lavas, respectively. The error bars of Nd isotopes represent $\pm$ 2σ propagated error using the external precision of the La Jolla standard ($\pm$0.000007) unless the internal precision of the single analysis was worse. Sr isotope error bars have been calculated using the same procedure but are not reported because they are within symbol size.

the whole rock (*e.g.*, Bea *et al.*, 1994; Ayres & Harris, 1997; Förster, 1998; Muñoz-Espadas *et al.,* 2000; Pyle *et al.*, 2001), determining a balancing effect in terms of Nd isotope composition in the analysed glass and mineral phases, including the HCl-leachates and the single grains phosphatic inclusions (Fig. 7).

6. Conclusions

In the present study, we have assessed the importance of minerals not attaining radiogenic isotope (Sr and Nd) equilibrium during crustal anatexis. The research has been focussed on the crustal xenoliths enclosed in the El Hoyazo and Mazarrón dacites of the Neogene Volcanic Province of SE Spain. The xenoliths represent a rather unique occurrence of *erupted melanosomes* from a migmatite complex: they experienced a melting episode that eventually determined the extraction of most of the anatectic liquid although some liquid remained as melt inclusions in the residual minerals. The outpouring of the dacitic lavas with the enclosed xenoliths froze the entrapped melt inclusions and has enabled us to study crustal melting in a geologic setting with clear source-melt relationship.

The anatectic system – residual crustal rocks and rhyolitic melts – remained at high-T (*ca.* 850 °C) for *ca.* 3 Myr at El Hoyazo and <0.8 Myr at Mazarrón (Cesare *et al.*, 2003a). These two different timescales are likely to resemble the generation of granites *s.l.* during rapid anatexis caused by basalt underplating (*e.g.*, England & Thompson, 1984; Huppert & Sparks, 1988).

Sr and Nd isotopes of minerals and melt inclusions in both localities did not attain isotopic equilibrium on a handspecimen (a few dm^3 scale. The isotopic disequilibrium is most marked in the Mazarrón xenolith, in keeping with the shorter residence time of the melt within the source, but, quite unexpectedly, isotopic disequilibrium (mainly $^{87}Sr/^{86}Sr$) is observed also in the El Hoyazo xenolith despite the longer residence time of the melt in the crust. The isotopic disequilibrium is not caused by the major xenolith-forming minerals but rather by the accessory phosphate inclusions (apatite $\pm$ monazite $\pm$ xenotime) hosted in garnet and biotite. The isotopic equilibration of these accessory phases, in addition to their intrinsically low Sr and Nd diffusion coefficients, has been further obstacolated by the armouring effect caused by their occurrence within biotite and garnet crystals, which acted as chemical barriers to Sr and Nd diffusion. This means that in natural rocks, modelling of radiogenic isotope equilibration cannot be simulated by considering a solid immersed in an infinite reservoir. More realistic modelling should consider elemental diffusion in a composite medium with a resistance at the interface, *i.e.* different partition coefficients between adjacent mineral phases (*e.g.*, Crank, 1975).

As a corollary, the result of this study indicates that a full assessment of both the timescales of crustal melting (Harris *et al.*, 2000) and the extent of radiogenic isotope (dis)equilibrium in crustal rocks during high-grade thermal events is critical to our understanding of granite petrogenesis and crustal growth processes. For example, crustal anatexis by basalt underplating is a rapid process, and is therefore liable to produce melts in radiogenic isotope disequilibrium with their sources. Equally, current models for assimilation of crustal material by basalts (*e.g.*, DePaolo, 1981) may need to be re-considered in the light of the potential role of minerals not attaining isotopic equilibrium.

References

Acosta-Vigil, A., Cesare, B., London, D., Morgan, G.B. (2007): Microstructures and composition of melt inclusions in a crustal anatectic environment: the metapelitic enclaves within El Hoyazo dacites, SE Spain. *Chem. Geol.*, **237**, 450–465.

Álvarez-Valero, A.M. (2004): Petrographic and thermodynamic study of the partialmelting of restitic xenoliths from the Neogene Volcanic Province of SE Spain. Unpublished Ph.D. thesis, Padova University, 223 p.

Álvarez-Valero, A.M., Cesare, B., Kriegsman, L.M. (2007): Formation of meltbearing spinel-cordierite-feldspars coronas after garnet in metapelitic xenoliths. Reaction modelling and geodynamic implications. *J. Metamorph. Geol.*, **25**, 305–320.

Anczkiewicz, R. & Thirlwall, M.F. (2003): Improving precision of the Sm-Nd garnet dating by H_2SO_4 leaching – a simple solution to phosphate inclusions problem. *in* ''Geochronology: linking the isotopic record with petrology and textures'', D. Vance, W. Müller, I.M. Villa, eds. *Geol. Soc. Lond. Spec. Pub.*, **220**, 83–91.

Avanzinelli, R., Boari, E., Conticelli, S., Francalanci, L., Guarnieri, L., Perini, G., Petrone, C. M., Tommasini, S., Ulivi, M. (2005): High precision Sr, Nd, and Pb isotopic analyses using new generation Thermal Ionisation Mass Spectrometer: aims and perspective for Isotope Geology Applications. *Periodico di Mineralogia*, **74**, 147–166.

Ayres, M. & Harris, N. (1997): REE fractionation and Nd-isotope disequilibrium during crustal anatexis: constraints from Himalayan leucogranites. *Chem. Geol.*, **139**, 249–269.

Banda, E., Gallart, J., García-Dueñas, V., Dañobeitia, J.J., Makris, J. (1993): Lateral variation of the crust in the Iberian Peninsula: New evidence from the Betic Cordillera. *Tectonophysics*, **221**, 53–66.

Barbero, L., Villaseca, C., Rogers, G., Brown, P.E. (1995): Geochemical and isotopic disequilibrium in crustal melting: an insight from the anatectic granitoids from Toledo, Spain. *J. Geophys. Res.*, **100**, 15745–15765.

Bea, F., Pereira, M.D., Strob, A. (1994): Mineral/leucosome trace-element partitioning in a peraluminous migmatite (a laser ablation-ICP-MS study). *Chem. Geol.*, **117**, 291–312.

Benito, R., López-Ruiz, J., Cebriá, J.M., Hertogen, J., Doblas, M., Oyarzun, R., Demaiffe, D. (1999): Sr and O isotope constraints on source and crustal contamination in the high-K calc-alkaline and shoshonitic neogene volcanic rocks of SE Spain. *Lithos*, **46**, 773–802.

Boynton, W.V. (1984): Cosmochemistry of the rare earth elements: meteorite studies. *in* ''Rare Earth Element Geochemistry'', P. Henderson, ed., Elsevier, Amsterdam, 63–114.

Burton, K.W., Kohn, M.J., Cohen, A.S., O'Nions, R.K. (1995): The relative diffusion of Pb, Nd, Sr and O in garnet. *Earth Planet. Sci. Lett.*, **133**, 199–211.

Cesare, B., Salvioli Mariani, E., Venturelli, G. (1997): Crustal anatexis and melt segregation in the restitic xenoliths at El Hoyazo (SE Spain). *Mineral. Mag.*, **61**, 15–27.

Cesare, B., Gómez-Pugnaire, M.T., Rubatto, D. (2003a): Residence time of S-type anatectic magmas beneath the Neogene Volcanic Province of SE Spain: a zircon and monazite SHRIMP study. *Contrib. Mineral. Petrol.*, **146**, 28–43.

Cesare, B., Cruciani, G., Russo, U. (2003b) Hydrogen deficiency in Ti-rich biotite from anatectic metapelites (El Joyazo – SE Spain): crystal-chemical aspects and implications for high-temperature petrogenesis. *Am. Mineral.*, **88**, 583–595.

Cesare, B., Meli, S., Nodari, L., Russo, U. (2005): Fe^{3+} reduction during biotite melting in graphitic metapelites: another origin of CO_2 in granulites. *Contrib. Mineral. Petrol.*, **149**, 129–140.

Cherniak, D.J. (1996): Sr diffusion in sanidine and albite and general comments on Sr diffusion in alkali feldspar. *Geochim. Cosmochim. Acta*, **60**, 5037–5043.

— (2000): Rare earth element diffusion in apatite. *Geochim. Cosmochim. Acta*, **22**, 3871–3885.

Cherniak, D.J. & Watson, E.B. (1992): A study of strontium diffusion in K-feldspar, Na-K feldspar and anorthite using Rutherford backscattering spectroscopy. *Earth Planet. Sci. Lett.*, **113**, 411–425.

Cherniak, D.J. & Ryerson, F.J. (1993): A study of strontium diffusion in apatite using Rutherford Backscattering spectroscopy and ion implantation. *Geochim. Cosmochim. Acta*, **57**, 4653–4662.

Crank, J. (1975): The mathematics of diffusion. Clarendon press, Oxford.

Davies, G.R., Halliday, A.N., Mahood, G.A., Hall, C.M. (1994): Isotopic constraints on the production rates, crystallisation histories and residence times of pre-caldera silicic magmas, Long Valley, California. *Earth Planet. Sci. Lett.*, **125**, 17–37.

DePaolo, D.J. (1981): Trace element and isotopic effects of combined wallrock assimilation and fractional crystallisation. *Earth Planet. Sci. Lett.*, **53**, 189–202.

De Wolf, C.P., Zeissler, C.J., Halliday, A.N., Mezger, K., Essene, E.J. (1996): The role of inclusions in U-Pb and Sm-Nd garnet geochronology: stepwise dissolution experiments and trace uranium mapping by fission track analysis. *Geochim. Cosmochim. Acta*, **60**, 121–134.

Duggen, S., Hoernle, K., van den Bogaard, P., Harris, C. (2004): Magmatic evolution of the Alboran region: the role of subduction in forming the western Mediterranean and causing the Messinian Salinity Crisis. *Earth Planet. Sci. Lett.*, **218**, 91–108.

Duggen, S., Hoernle, K., van den Bogaard, P., Garbe-Schönberg, D. (2005): Post-collisional transition from subduction- to intraplate-type magmatism in the westernmost Mediterranean: evidence for continental-edge delamination of the subcontinental lithosphere. *J. Petrol.*, **46**, 1155–1201.

England, C. & Thompson, A.B. (1984): Pressure-Temperature-Time Paths of regional metamorphism I. Heat transfer during the evolution of regions of thickened continental crust. *J. Petrol.*, **25**, 894–928.

Ferri, F, Burlini, L., Cesare, B., Sassi, R. (2007): Seismic properties of lower crustal xenoliths from El Hoyazo (SE Spain). Experimental evidence up to partial melting. *Earth Planet. Sci. Lett.*, **253**, 239–253.

Förster, H.J. (1998): The chemical composition of REE-Y-Th-U-rich accessory minerals in peraluminous granites of the Erzgebirge-Fichtelgerbirge region, Germany. Part II: xenotime. *Am. Mineral.*, **83**, 1302–1315.

Giletti, B.J. (1991): Rb and Sr diffusion in alklai feldspars, with implications for cooling histories of rocks. *Geochim. Cosmochim. Acta*, **55**, 1331–1343.

Halliday, A.N., Mahood, G.A., Holden, P., Metz, J.M., Dempster, T.J., Davidson, J.P. (1989): Evidence for long residence times of rhyolitic magma in the Long Valley magmatic system: the isotopic record in precaldera lavas of Glass Mountain. *Earth Planet. Sci. Lett.*, **94**, 274–290.

Hammouda, T., Pichavant, M., Chaussidon, M. (1996): Isotopic equilibration during partial melting: an experimental test of the behaviour of Sr. *Earth Planet. Sci. Lett.*, **144**, 109–122.

Harris, N. & Ayres, M. (1998): The implications of Sr-isotope disequilibrium for rates of prograde metamorphism and melt extraction in anatectic terrains. *in* ''What drives metamorphism and metamorphic reactions?'', P.J. Treloar & P.J. O'Brien, eds. *Geol. Soc. Lond. Spec. Pub.*, **138**, 171–182.

Harris, N., Vance, D., Ayres, M. (2000): From sediment to granite: timescales of anatexis in the upper crust. *Chem. Geol.*, **162**, 155–167.

Huppert, H.E. & Sparks, R.S. (1988): The generation of granitic magmas by intrusion of basalt into continental crust. *J. Petrol.*, **29**, 99–624.

Julià, J., Mancilla, F., Morales, J. (2005): Seismic signature of intracrustal magmatic intrusions in the Eastern Betics (Internal Zone), SE Iberia. *Geophys. Res. Lett.*, **32**, L16304, doi:10.1029/2005GL023274.

Jung, S. & Mezger, K. (2003): Petrology of basement-dominated terranes: I. Regional metamorphic T-*t* path from U-Pb monazite and Sm-Nd garnet geochronology (Central Damara orogen, Namibia). *Chem. Geol.*, **198**, 223–247.

Knesel, K.M. & Davidson, J.P. (2002): Insights into collisional magmatism from isotopic fingerprints of melting reactions. *Science*, **296**, 2206–2208.

Kretz, R. (1983): Symbols for rock-forming minerals. *Am. Mineral.*, **68**, 277–279.

López-Ruiz, J., Cebriá, J.M., Doblas, M. (2002): Cenozoic volcanism I: the Iberian Peninsula. *in* ''Geology of Spain'', W. Gibbons & T. Moreno, eds. *Geol. Soc. Lond.*, 417–438.

Munksgaard, N.C., (1985): A non-magmatic origin for compositionally zoned euhedral garnets in silicic Neogene volcanics from SE Spain. *Neues Jahrb. Mineral. Mh.*, **2**, 73–82.

Muñoz-Espadas, M.J., Lunar, R., Martínez-Frías, J. (2000): The garnet placer deposit from SE Spain: industrial recovery and geochemical features. *Episodes*, **23**, 266–269.

Peccerillo, A. & Taylor, S.R. (1976): Geochemistry of Eocene calc-alkaline volcanic rocks from the Kastamonu area, northern Turkey. *Contrib. Mineral. Petrol.*, **58**, 63–81.

Prowatke, S. & Klemme, S. (2006): Trace element partitioning between apatite and Silicate melts. *Geochim. Cosmochim. Acta*, **70**, 4513–4527.

Pyle, J.M., Spear, F.S., Rudnick, R.L., McDonough, W.F. (2001): Monazite-Xenotime-Garnet equilibrium in metapelites and a new Monazite-Garnet thermometer. *J. Petrol.*, **42**, 2083–2107.

Tommasini, S. & Davies, G.R. (1997): Isotope disequilibrium during anatexis: a case study of contact melting, Sierra Nevada, CA. *Earth Planet. Sci. Lett.*, **148**, 273–285.

Torné, M., Fernández, M., Comas, M.C., Soto, J.I. (2000): Lithospheric structure beneath the Alboran basin: results from 3D gravity modeling and tectonic relevance. *J. Geophys. Res.*, **105**, 3209–3228.

Turner, S.P., Platt, J.P., George, R.M.M., Kelley, S.P., Pearson, D.G., Nowell, G.M. (1999): Magmatism associated with orogenic collapse of the Betic-Alboran Domain, SE Spain. *J. Petrol.*, **40**, 1011–1036.

Zeck, H.P. (1968): Anatectic origin and further petrogenesis of almandine-bearing biotite–cordierite–labradorite dacite with many inclusions of restite and basaltoid material, Cerro de Hoyazo, SE Spain. Unpublished PhD Thesis, Amsterdam, 162 p.

— (1970): An erupted migmatite from Cerro de Hoyazo, SE Spain. *Contrib. Mineral. Petrol.*, **26**, 225–246.

Zeck, H.P. & Williams, I.S. (2002): Inherited and magmatic zircon from neogene Hoyazo Cordierite Dacite, SE Spain – anatectic source rock provenance and magmatic evolution. *J. Petrol.*, **43**, 1089–1104.

Zeck, H.P., Kristensen, A.B., Nakamura, E. (1999): Inherited Paleozoic and Mesozoic Rb-Sr isotopic signatures in Neogene Calc-alkaline volcanics, Alboran Volcanic Province, SE Spain. *J. Petrol.*, **40**, 511–524.

Zeng, L., Asimow, P.D., Saleeby, J.B. (2005a): Coupling of anatectic reactions and dissolution of accessory phases and the Sr and Nd isotope systematics of anatectic melts from a metasedimentary source. *Geochim. Cosmochim. Acta*, **69**, 3671–3682.

Zeng, L., Saleeby, J.B., Ducea, M. (2005b): Geochemical characteristics of crustal anatexis during the formation of migmatite at the Southern Sierra Nevada, California. *Contrib. Mineral. Petrol.*, **150**, 386–402.

Zeng, L., Saleeby, J.B., Asimow, P. (2005c): Nd isotope disequilibrium during crustal anatexis: a record from the Goat Ranch migmatite complex, southern Sierra Nevada batholith, California. *Geology*, **33**, 53–56.